J. Fluid Mech. (2018), *vol.* 853, *pp.* 461–487.
doi:10.1017/jfm.2018.572

A volume integral implementation of the Goldstein generalised acoustic analogy for unsteady flow simulations

Vasily A. Semiletov[1,2] **and Sergey A. Karabasov**[1,2,†]

[1]School of Engineering and Materials Science, Queen Mary University of London, London E1 4NS, UK

[2]GPU-Prime Ltd, Cambridge CB23 7DN, UK

(Received 14 January 2018; revised 8 May 2018; accepted 16 July 2018;
first published online 23 August 2018)

A new volume integral method based on the Goldstein generalised acoustic analogy is developed and directly applied with large-eddy simulation (LES). In comparison with the existing Goldstein generalised acoustic analogy implementations, the current method does not require the computation and recording of the expensive fluctuating stress autocovariance function in the seven-dimensional space–time. Until now, the multidimensional complexity of the generalised acoustic analogy source term has been the main barrier to using it in routine engineering calculations. The new method only requires local pointwise stresses as an input that can be routinely computed during the flow simulation. On the other hand, the new method is mathematically equivalent to the original Goldstein acoustic analogy formulation, and, thus, allows for a direct correspondence between different effective noise sources in the jet and the far-field noise spectra. The implementation is performed for conditions of a high-speed subsonic isothermal jet corresponding to the Rolls-Royce SILOET experiment and uses the LES solution based on the CABARET solver. The flow and noise solutions are validated by comparison with experiment. The accuracy and robustness of the integral volume implementation of the generalised acoustic analogy are compared with those based on the standard Ffowcs Williams–Hawkings surface integral method and the conventional Lighthill acoustic analogy. As a demonstration of its capabilities to investigate jet noise mechanisms, the new integral volume method is applied to analyse the relative importance of various noise generation and propagation components within the Goldstein generalised acoustic analogy model.

Key words: aeroacoustics, computational methods, jet noise

1. Introduction

The theoretical study of jet noise was pioneered by Lighthill (1952), who proposed the first acoustic analogy model. The Lighthill model is as an exact rearrangement of the Navier–Stokes equations into a linear wave propagation operator and a nominal source term. All of the terms of the Navier–Stokes equations not included in the wave operator are grouped together in the source term and expressed as the gradient

† Email address for correspondence: s.karabasov@qmul.ac.uk

of the Lighthill stress tensor. The latter tensor includes both the nonlinear velocity stress, $\rho v'_i v'_j$, which gives rise to the quadrupole-type source, and the linear terms, $\rho \bar{v}_i v'_j + \rho \bar{v}_j v'_i$ and $(p' - c_\infty^2 \rho')\delta_{ij}$, the so-called 'shear noise' and 'entropy noise' terms respectively. Here, the standard notations of time-averaged field and fluctuations with overbar and prime respectively are used; c_∞ is the sound speed in the free stream, v_i is the velocity component in the i direction of the Cartesian coordinate basis $i, j = 1, 2, 3$, ρ is density and p is pressure. The presence of the linear terms, which contain linear mean-flow sound propagation and temperature effects, leads to differences in Mach number scaling compared with the sound generated by the nonlinear quadrupole term alone, which corresponds to the celebrated Lighthill v^8 law for the far-field sound power (Viswanathan 2009; Semiletov & Karabasov 2017).

Since Lighthill, major developments of the acoustic analogy method include those of Curle (1955), who considered the effect of solid surfaces, Lilley (1958), who took into account mean-flow sound refraction effects, and Ffowcs Williams (1963), who correctly accounted for the effect of moving sound sources. Goldstein (2002, 2003) proposed the generalised acoustic analogy to account for mean-flow propagation effects by exactly rearranging the governing Navier–Stokes equations into a linear hyperbolic part and the nonlinear acoustic source term which only involves nonlinear stresses, which are expressed in terms of a fluctuation and have zero mean, which is a significant improvement over the previous acoustic analogy models.

Early work on idealised flow problems (e.g. Samanta *et al.* 2006) showed that the Goldstein generalised acoustic analogy has great promise for use in unsteady flow simulations as it has the lowest sensitivity to source errors compared with the classical Lighthill or Lilley models. However, to date, the main applications of the generalised analogy have been limited to the class of 'low-order' noise prediction schemes which use various approximate models to represent the acoustic source strengths (e.g. Goldstein & Leib 2008; Goldstein 2011; Leib & Goldstein 2011; Goldstein, Sescu & Afsar 2012); these approximations have been 'informed' by large-eddy simulation (LES) or direct numerical simulation (DNS) in other works (e.g. Karabasov *et al.* 2010; Karabasov, Bogey & Hynes 2013; Depuru Mohan *et al.* 2015; Karabasov & Sandberg 2015).

The frequent use of approximations can be explained by the fact that the Goldstein generalised acoustic analogy model was originally formulated as an integral relation between the autocovariance of fluid stresses and the far-field sound. This relation requires the computation and storage of the corresponding autocorrelation tensor, such as the fourth-order velocity autocorrelation functions for the isothermal jet case, in a seven-dimensional space–time. The fourth-rank autocorrelation tensor corresponding to the source term of the generalised acoustic analogy is built from a stress tensor $e''_{\mu j}$ of dimension (4×3), which has nine different components, and the total number of different components of the autocorrelation tensor for asymmetric jet flows is $\sum_1^9 n = 45$. For axisymmetric jets, under some reasonable assumptions about symmetry of the turbulence, the number of different source terms can be reduced to 11 independent components (Afsar, Goldstein & Fagan 2011), which is still a significant number. The resulting source complexity makes direct evaluation of the entire statistical source from unsteady flow simulations extremely challenging.

On the other hand, unsteady flow simulation methods like LES or hybrid Reynolds-averaged Navier–Stokes (RANS)–LES have gained popularity for jet noise prediction (Shur, Spalart & Strelets 2005; Faranosov *et al.* 2013; Shur *et al.* 2015) when applied with integral surface formulations such as those of Kirchhoff or Ffowcs Williams & Hawkings (1969) (e.g. di Francescantonio 1997; Brentner & Farassat

1998; Najafi-Yazdi, Bres & Mongeau 2011) due to the simplicity and efficiency of the latter formulations. In principle, the availability of time-dependent three-dimensional flow data at high resolution from unsteady flow simulations allows one to investigate jet noise mechanisms at a new level of detail compared with the current space–time resolution available in experimental studies (e.g. Bridges 2010; Morris & Zaman 2010). However, computational models based on surface integral formulations tend to be sensitive to the formulation of the far-field propagation model as well as the location and configuration details of the integration surface. Furthermore, compared with volume integral methods, integral surface methods offer no insight into the actual noise sources in the jet.

Volume integral methods based on the Lighthill acoustic analogy and unsteady flow simulations have also found use for jet noise modelling. For example, in Freund (2003) and Bogey & Bailly (2010), DNS and LES solutions respectively of high-speed jet flows were used to compute the Lighthill stress terms, which were then substituted in the acoustic integral to calculate the far-field pressure and the corresponding far-field sound power. The computations involved recording the local stress quantities in the jet volume, which is a considerably simpler task compared with computing the autocovariance function of the corresponding stresses. However, for sound predictions based on the LES, which had to resolve a mixture of sound generation and propagation effects that appear in the definition of the Lighthill stress, large errors in overall sound pressure levels were reported. This revealed the importance of explicitly representing linear mean-flow propagation effects in the acoustic analogy equations, which are partially accounted for in the Lilley acoustic analogy and, most consistently, in the Goldstein generalised acoustic analogy (for a detailed discussion of the differences between the two analogies, see Goldstein (2010)).

In Semiletov & Karabasov (2014*a*,*b*) and Semiletov *et al.* (2015), the idea of computing the local stresses inside the jet volume and then reconstructing the far-field pressure and the corresponding sound power was extended to the Goldstein generalised acoustic analogy equations. In comparison with previous implementations of the generalised acoustic analogy based on recording the fourth-order velocity autocorrelation functions, this approach is straightforward for computational implementation and does not require any simplifying assumptions about the effective source configuration in the multidimensional space–time. The current article not only provides a systematic and expanded review of these developments but also presents new results of the effective noise source analysis in accordance with the following plan.

In § 2, the Goldstein generalised acoustic analogy is briefly reviewed and its implementation as a volume integral method is introduced. In § 3, details of the SILOET benchmark jet case which is used for validation of the method developed is considered, the LES method is introduced, and the flow and noise solutions are compared with available data in the literature and other reference computations. Section 4 is devoted to analysis of sound generation and propagation mechanisms based on the volume integral formulation of the Goldstein generalised acoustic analogy developed.

2. Goldstein generalised acoustic analogy

2.1. *Formulation based on the autocovariance of generalised flow stresses*

Following Goldstein & Leib (2008), time-averaged, Favre-averaged mean-flow and fluctuation variables are introduced,

$$\rho' = \rho - \overline{\rho}, \quad p' = p - \overline{p}, \quad h' = h - \overline{h}, \quad v_i' = v_i - \overline{v}_i, \tag{2.1a–d}$$

where ρ, p, v and h refer to density, pressure, velocity and enthalpy respectively; primes denote fluctuations, and bars and tildes correspond to time and Favre averaging.

By defining the new dependent variables

$$\left.\begin{array}{c} p'_e = p' + \dfrac{\gamma-1}{2}(\rho v'^2 - \overline{\rho}\widetilde{v'^2}), \\ u_i = \rho v'_i, \end{array}\right\} \tag{2.2}$$

the governing Navier–Stokes equations are exactly rearranged to

$$\left.\begin{array}{c} D_0\rho' + \nabla_j u_j = 0, \\ D_0 u_i + u_i\nabla_j\widetilde{v}_j + \nabla_i p'_e - \dfrac{\rho'}{\overline{\rho}}\nabla_j\widetilde{\theta}_{ij} = \nabla_j e''_{ij}, \\ D_0 p'_e + \nabla_j\widetilde{c^2}u_j + (\gamma-1)\left(p'_e\nabla_j\widetilde{v}_j - \dfrac{u_i}{\overline{\rho}}\nabla_j\widetilde{\theta}_{ij}\right) = \nabla_j e''_{4j} + (\gamma-1)e''_{ij}\nabla_j\widetilde{v}_i, \end{array}\right\} \tag{2.3}$$

where

$$\nabla_j = \frac{\partial\cdot}{\partial y_j}, \quad D_0 = \frac{\partial}{\partial t}\cdot + \nabla_j(\widetilde{v}_j\cdot) \tag{2.4a,b}$$

and

$$\left.\begin{array}{c} e''_{\mu j} = e'_{\mu j} - \overline{e'_{\mu j}}, \quad \widetilde{\theta}_{\mu j} = \delta_{\mu j}\overline{p}_e - \overline{e'_{\mu j}}, \\ e'_{\mu j} = -\rho v'_\mu v'_j + \delta_{\mu j}\dfrac{\gamma-1}{2}v'^2 + (\sigma_{\mu j} + (\gamma-1)\delta_{\mu 4}\sigma_{jk}v'_k), \\ v'_4 = (\gamma-1)\left(h' + \dfrac{1}{2}v'^2\right) = (c^2)' + \dfrac{\gamma-1}{2}v'^2, \quad \sigma'_{4j} = -(\gamma-1)q_j, \\ i,j = 1,2,3; \quad \mu = 1,2,3,4. \end{array}\right\} \tag{2.5}$$

In the above equations, Einstein summation is implied, σ_{ij} and q_j are the viscous stress and heat flux respectively, $\widetilde{c^2}$ is the square of the mean-flow sound speed, which is used to define the corresponding fluctuation, $\widetilde{\theta}_{ij}$ is the total mean-flow stress tensor and $e''_{\mu j}$ is the generalised fluctuating stress tensor. It should be noted that the latter (4×3) tensor includes both the fluctuating Reynolds stresses and the fluctuating enthalpy vector. This is the same term that appears as a separate source component in other formulations of the generalised acoustic analogy (Goldstein 2002, 2003, 2011).

By introducing the far-field microphone and the jet flow coordinates, $\boldsymbol{x}$ and $\boldsymbol{y}$ respectively, the spectral density of the far-field pressure signal can be expressed as the acoustic integral

$$S(\boldsymbol{x},\omega) = \int_{V_y}\int_{V_\Delta} \hat{R}_{\mu jkl}(\boldsymbol{y},\boldsymbol{\Delta},\omega)\hat{\gamma}_{\mu j}(\boldsymbol{y},\omega|\boldsymbol{x})\hat{\gamma}^*_{kl}(\boldsymbol{y}+\boldsymbol{\Delta},\omega|\boldsymbol{x})\,\mathrm{d}\boldsymbol{\Delta}\,\mathrm{d}\boldsymbol{y} \tag{2.6}$$

of the generalised stress tensor autocovariance

$$\hat{R}_{\mu jkl}(\boldsymbol{y},\boldsymbol{\Delta},\omega) = \int R_{\mu jkl}(\boldsymbol{y},\boldsymbol{\Delta},\tau)\mathrm{e}^{-\mathrm{i}\omega\tau}\,\mathrm{d}\tau. \tag{2.7}$$

Here, $R_{\mu jkl}(\boldsymbol{y},\boldsymbol{\Delta},\tau) = \overline{e''_{\mu j}(\boldsymbol{y},\tau)e''^*_{kl}(\boldsymbol{y}+\boldsymbol{\Delta},t+\tau)}$ is the generalised stress tensor autocovariance in the time domain, where the overbar means averaging over time t, $i,j = 1,2,3$ and $\mu,k = 1,2,3,4$.

It is the time-domain generalised stress tensor autocovariance that can, in principle, be provided from unsteady flow simulations. However, since it is a fourth rank tensor defined over the entire $(6+1)$-dimensional space–time domain, computation of this quantity is a challenge.

Using the standard Fourier transformation formulae, the same quantity can be related to the frequency-domain representation of the stresses,

$$\hat{R}_{ijkl}(\boldsymbol{y}, \boldsymbol{\Delta}, \omega) = \overline{\hat{e}''_{ij}(\boldsymbol{y}, \omega)\hat{e}''^{*}_{kl}(\boldsymbol{y}+\boldsymbol{\Delta}, \omega)}, \quad \text{where } \hat{e}_{ij}(\boldsymbol{y}, \omega) = \int e_{ij}(\boldsymbol{y}, \tau)\mathrm{e}^{-\mathrm{i}\omega\tau}\,\mathrm{d}\tau. \tag{2.8}$$

The other part of the far-field sound integral (2.6) is the propagator operator,

$$\left.\begin{gathered}\hat{\gamma}_{ij}(\boldsymbol{y}, \omega|\boldsymbol{x}) = \nabla_i \hat{u}^a_j(\boldsymbol{y}, \omega|\boldsymbol{x}) + \hat{p}^a(\boldsymbol{y}, \omega|\boldsymbol{x})\nabla_j \widetilde{v}_i(\boldsymbol{y}), \\ \hat{\gamma}_{4j}(\boldsymbol{y}, \omega|\boldsymbol{x}) = -\nabla_j \hat{p}^a(\boldsymbol{y}, \omega|\boldsymbol{x}),\end{gathered}\right\} \tag{2.9}$$

which depends on the corresponding adjoint vector Green's function, $(\hat{\boldsymbol{u}}^a(\boldsymbol{y}, \omega|\boldsymbol{x}), \hat{p}^a(\boldsymbol{y}, \omega|\boldsymbol{x}))$. The adjoint vector Green's function is directly related to the direct tensor Green's function in accordance with the reciprocal theorem between the solution of the direct sound radiation and the adjoint sound scattering problem (e.g. see Tam & Auriault 1998; Karabasov 2010). Compared with solution of the direct sound radiation problem, solution of the adjoint problem for a small number of far-field microphone locations relative to the number of source points is computationally advantageous. In the frequency domain, the latter is determined by the following adjoint linearised Euler equations:

$$\left.\begin{gathered}D_1\hat{\rho}^a + \frac{\hat{u}^a_i}{\overline{\rho}}\nabla_j\widetilde{\theta}_{ij} = 0, \\ D_1\hat{u}^a_i + \nabla_i\hat{\rho}^a - \hat{u}^a_i\nabla_j\widetilde{v}_j + \widetilde{c^2}\nabla_j\hat{p}^a + \hat{p}^a\frac{\gamma-1}{\overline{\rho}}\nabla_j\widetilde{\theta}_{ij} = 0, \\ D_1\hat{p}^a + \nabla_j\hat{u}^a_j - (\gamma-1)\hat{p}^a\nabla_j\widetilde{v}_j = \delta(\boldsymbol{y}-\boldsymbol{x}),\end{gathered}\right\} \tag{2.10}$$

where

$$D_1 = \mathrm{i}\omega\cdot + \widetilde{v}_j\nabla_j(\cdot). \tag{2.11}$$

The solution of these equations can be found by numerically solving the above equations with the delta function source term replaced by an appropriate open-domain radiation boundary condition corresponding to a sink in the far-field observer location (Karabasov & Hynes 2006). The current work, following Tam & Auriault (1998) and Semiletov *et al.* (2015), uses a simplified semianalytical locally parallel flow approximation to solve the sound mean-flow propagation problem. Briefly, under the locally parallel flow approximation, the jet flow is divided into a series of non-overlapping sections along the jet streamwise coordinate. Each of the sections is streamwise averaged to correspond to a piecewise constant flow field in terms of the streamwise coordinate which becomes a function of radius only, i.e. $\widetilde{v} = (\widetilde{v}(r), 0, 0)$, $\widetilde{c} = \widetilde{c}(r)$, of the cylindrical–polar coordinate basis in the jet $\boldsymbol{y} = (r, \theta, z)$. For each jet section, periodic boundary conditions are assumed in the streamwise z direction. After such simplifications, the linearised Euler equations can be decomposed into equations for each azimuthal mode separately. This leads to an ordinary differential equation of Rayleigh type for the amplitude of each mode as a function of radius to be solved numerically. Overall, the solution for the amplitudes

will be a function of both radius and axial location because of the local mean-flow velocity profile used.

It can be remarked that in a number of previous publications (Afsar, Sescu & Leib 2016; Goldstein & Leib 2016), including some earlier work of the present authors (Karabasov *et al.* 2010, 2013), the importance of a fully evolving flow/sound propagation model for far-field jet noise predictions was stressed. While the effect of a more accurate definition of the Green's function, taking jet flow evolution effects into account, compared with the locally parallel flow model will be a subject of future investigations, the present work is the first in the literature where the effective source term is evaluated directly from LES, avoiding the approximations of previous models. Hence, it is possible that the far-field acoustic solutions, which were obtained in the earlier works as convolution products of the Green's function propagator with an approximate model of the seven-dimensional space–time source term, could have a larger sensitivity to the evolving jet mean-flow details compared with the present approach which is approximation-free.

2.2. *Formulation based on the volume integral approach*

The same far-field power spectral density (2.6) can be expressed as a complex conjugate of the far-field pressure,

$$S(\boldsymbol{x}, \omega) = \overline{\hat{p}(\boldsymbol{x}, \omega)\hat{p}^*(\boldsymbol{x}, \omega)}, \tag{2.12}$$

where $\hat{p}(\boldsymbol{x}, \omega)$ is the frequency-domain pressure signal at the far-field microphone location and the overbar indicates statistical ensemble averaging.

In turn, the frequency-domain pressure signal can be expressed as a volume integral of the source and the vector adjoint Green's function that satisfies (2.10) and (2.11). After some rearrangement involving a few integrations by parts, this leads to

$$\begin{aligned}\hat{p}(\boldsymbol{x}, \omega) \;=\; \int_{V_y} \Big\{ & \hat{e}''_{ij}(\boldsymbol{y}, \omega)\nabla_i \hat{u}^a_j(\boldsymbol{y}, \omega|\boldsymbol{x}) - \frac{\mathrm{i}\omega}{\widetilde{c^2}}\left(\hat{e}''_{4j}(\boldsymbol{y}, \omega)\nabla_j \hat{p}^a(\boldsymbol{y}, \omega|\boldsymbol{x})\right. \\ & \left. - \;(\gamma-1)\hat{e}''_{ij}(\boldsymbol{y}, \omega)\nabla_j \widetilde{v}_i(\boldsymbol{y})\hat{p}^a(\boldsymbol{y}, \omega|\boldsymbol{x})\right) \Big\}\, \mathrm{d}\boldsymbol{y}, \quad i, j = 1, 2, 3. \end{aligned} \tag{2.13}$$

Let us assume that $\boldsymbol{e}_1$ is the Cartesian coordinate in the streamwise (jet flow) direction, $(\boldsymbol{e}_2, \boldsymbol{e}_3)$ are in the transverse plane and $(\boldsymbol{e}_1, \boldsymbol{e}_2)$ are in plane with the far-field microphone.

There are three types of noise sources that can be identified in (2.13): (i) the fluctuating Reynolds stress $\hat{e}''_{ij}(\boldsymbol{y}, \omega)$, (ii) the fluctuating stagnation enthalpy stress $(\omega/\widetilde{c^2})\hat{e}''_{4j}(\boldsymbol{y}, \omega)$ and (iii) a term associated with the non-divergent mean-flow velocity field $(\omega(\gamma-1)/\widetilde{c^2})\hat{e}''_{ij}(\boldsymbol{y}, \omega)\nabla_j \widetilde{v}_i(\boldsymbol{y})$.

For an axisymmetric mean flow, the 3D integral can be further decomposed into a series of two-dimensional azimuthal modes,

$$\begin{aligned}\hat{p}(\boldsymbol{x}, \omega) = \sum_n \hat{p}^{(n)}(\boldsymbol{x}, \omega) = \sum_n \int_{V_{y\eta}} \{ & \hat{e}''^{(n)}_{ij}(\boldsymbol{y}_\eta, \omega)\nabla_i \hat{u}^{a(n)}_j(\boldsymbol{y}_\eta, \omega|\boldsymbol{x}) \\ & - \hat{e}''^{(n)}_{4j}(\boldsymbol{y}_\eta, \omega)\nabla_j \hat{p}^{a(n)}(\boldsymbol{y}_\eta, \omega|\boldsymbol{x}) - (\gamma-1)\hat{e}''^{(n)}_{ij}(\boldsymbol{y}_\eta, \omega)\nabla_j \widetilde{v}_i(\boldsymbol{y}_\eta)\hat{p}^{a(n)}(\boldsymbol{y}_\eta, \omega|\boldsymbol{x})\}\, \mathrm{d}\boldsymbol{y}_\eta, \end{aligned} \tag{2.14}$$

using the standard definition of the Fourier transform in the azimuthal direction,

$$f^{(n)}(\boldsymbol{y}_\eta) = \int_0^{2\pi} \mathrm{e}^{\mathrm{i}n\theta} f(z, r, \theta)\, \mathrm{d}\theta. \tag{2.15}$$

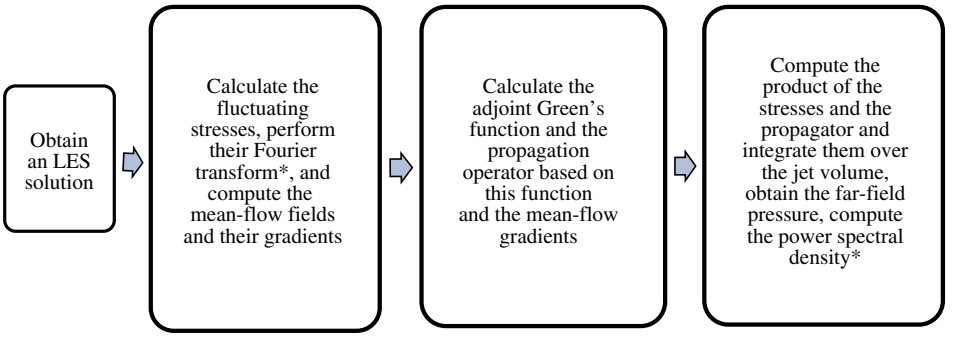

FIGURE 1. (Colour online) Flow diagram of the volume integral method based on the generalised acoustic analogy; * indicates the use of signal processing techniques to compensate for a finite duration of the LES time signal.

Here, $(\boldsymbol{y}_\eta, \theta) = (r, z, \theta)$ is a local cylindrical–polar coordinate basis in the jet, where r and θ are the radial and azimuthal angle components and z coincides with the jet axis. Vectors with superscript (n) correspond to the (r, z) components of the cylindrical–polar system. The modal representation is useful for reducing computer storage overheads when recording the stresses in the 3D jet volume since for axisymmetric jets it is only a relatively small number of modes (compared with the points of the LES grid) that can contribute efficiently to the acoustic integral.

Apparently, the method of computing the far-field spectral density based on the 3D volume integral formulation (2.12)–(2.14) is mathematically identical to the standard formulation (2.6)–(2.9). However, there is no calculation of the generalised stress tensor autocovariance involved in the former volume integral formulation, which leads to a considerable saving of computer memory resources compared with the standard approach. Table 1 compares the computer memory costs for recording the fluctuating stresses required for the volume integral formulation (2.6)–(2.9) with those of computing the generalised autocovariance stress tensor for the formulation (2.12)–(2.14). The figures are based on the jet case example to be considered in § 3. For simplicity, all numbers are normalised by the computational cost of the volume integral approach. It should be noted that even for a limited number of tensor components, the computation of the autocovariance function is five orders of magnitude more expensive than with the integral volume approach.

The total computer storage required with the current implementation of the volume integral method for the jet case considered is around 4 TB, which figure could be reduced by performing all preprocessing operations on the fly.

The implementation of the volume integral approach involves the following steps (figure 1).

(1) Perform an LES simulation.
(2) Calculate all 12 components of the fluctuating stress tensor, $e''_{\mu j}$, in the jet volume by applying (2.5).
(3) Fourier transform the stress components in time and in the azimuthal direction, record the several discrete frequencies and modes needed; for the processing of the LES time signals, use the signal processing theory (Welch 1967): (i) break each fluctuating stress signal into several subintervals with 50% overlap, (ii) Fourier transform each set and (iii) record them as several independent frequency-domain realisations of the stresses.

	Volume integral approach (2.6)–(2.9), all terms	Stress tensor autocoherence approach (2.12)–(2.14), 10 autocorrelation tensor components	Stress tensor autocoherence approach (2.12)–(2.14), all 45 autocorrelation tensor components
Cost	1	328 200	1476 900

TABLE 1. Computer memory costs of different implementations of the Goldstein generalised acoustic analogy.

(4) Calculate the mean jet flow properties.
(5) For each frequency and mode required, calculate the adjoint Green's function, $\hat{u}^{a(n)}(\boldsymbol{y}_\eta, \omega \,|\, \boldsymbol{x})$, $\hat{p}^{a(n)}(\boldsymbol{y}_\eta, \omega \,|\, \boldsymbol{x})$.
(6) For each set of the frequency-domain stress fields recorded, integrate the source over the 2D volume, V_{y_η}, and sum over all modes to obtain the far-field pressure signal (2.14) for each realisation.
(7) Calculate the power spectral density by averaging over all realisations of the frequency-domain stress fields available (2.12).

2.3. *Volume integral formulation and effective source decomposition*

Compared with the standard generalised acoustic analogy approach (2.12)–(2.14), which links the effective sources in the jet to the far-field sound power, the same direct correspondence is not explicit for the current volume integral formulation. Indeed, the current approach first relates the fluctuating stress terms in the jet to the far-field pressure and then relates the far-field pressure to the far-field sound.

To demonstrate how the analysis of far-field noise sources in the jet is also possible within the suggested volume integral approach, let us first decompose the far-field pressure integral into the contributions of individual modes and the corresponding modes of the vector adjoint Green's function terms using (2.14). For each mode, the far-field pressure integral can be further broken down into the contributions of different source components,

$$\left.\begin{aligned}
\hat{p}^{(n)}_{e_{ij}}(\boldsymbol{x}, \omega) &= \int_{V_y} \hat{e}''^{(n)}_{ij}(\boldsymbol{y}_\eta, \omega) \nabla_i \hat{u}^{a(n)}_j(\boldsymbol{y}_\eta, \omega|\boldsymbol{x}) \,\mathrm{d}\boldsymbol{y}_\eta, \\
\hat{p}^{(n)}_{e_{4j}}(\boldsymbol{x}, \omega) &= \int_{V_y} \hat{e}''^{(n)}_{4j}(\boldsymbol{y}_\eta, \omega) \nabla_j \hat{p}^{a(n)}(\boldsymbol{y}_\eta, \omega|\boldsymbol{x}) \,\mathrm{d}\boldsymbol{y}_\eta, \\
\hat{p}^{(n)}_{\nabla_j \widetilde{v}_i}(\boldsymbol{x}, \omega) &= \int_{V_y} (\gamma - 1) \hat{e}''^{(n)}_{ij}(\boldsymbol{y}_\eta, \omega) \nabla_j \widetilde{v}_i(\boldsymbol{y}_\eta) \hat{p}^{a(n)}(\boldsymbol{y}_\eta, \omega|\boldsymbol{x}) \,\mathrm{d}\boldsymbol{y}_\eta.
\end{aligned}\right\} \tag{2.16}$$

The contributions due to the fluctuating Reynolds stresses can be further decomposed into

$$\left.\begin{aligned}
\hat{p}^{(n)}_{e_{11}}(\boldsymbol{x}, \omega) &= \int_{V_y} \hat{e}''^{(n)}_{11}(\boldsymbol{y}_\eta, \omega) \nabla_1 \hat{u}^{a(n)}_1(\boldsymbol{y}_\eta, \omega|\boldsymbol{x}) \,\mathrm{d}\boldsymbol{y}_\eta, \\
\hat{p}^{(n)}_{e_{12}}(\boldsymbol{x}, \omega) &= \int_{V_y} \hat{e}''^{(n)}_{12}(\boldsymbol{y}_\eta, \omega) \nabla_1 \hat{u}^{a(n)}_2(\boldsymbol{y}_\eta, \omega|\boldsymbol{x}) \,\mathrm{d}\boldsymbol{y}_\eta, \\
\hat{p}^{(n)}_{e_{22}}(\boldsymbol{x}, \omega) &= \int_{V_y} \hat{e}''^{(n)}_{22}(\boldsymbol{y}_\eta, \omega) \nabla_2 \hat{u}^{a(n)}_2(\boldsymbol{y}_\eta, \omega|\boldsymbol{x}) \,\mathrm{d}\boldsymbol{y}_\eta,
\end{aligned}\right\} \tag{2.17}$$

and so on.

By disabling all source terms except from any user-defined stress and mode component of the pressure integral $\hat{p}(\boldsymbol{x}, \omega)$, the contribution of this particular source term in the far-field power spectra $\hat{P}(\boldsymbol{x}, \omega)$ can be calculated.

Furthermore, the effect of cross-products in the power spectra integral can be ignored; that is, only symmetric terms of the generalised stress tensor autocovariance, $R_{\mu j \mu j}$, are important for the far-field sound. The source symmetry property is consistent with observations made for other high-speed axisymmetric jets (e.g. compare with R_{1111}, R_{2222}, R_{3333}, R_{1212}, R_{1313} and R_{2323} main source components considered in Karabasov *et al.* (2010)) and the sound power spectra can be decomposed into the contributions of individual terms,

$$\begin{aligned}\hat{P}(\boldsymbol{x}, \omega) &= \sum_{n,m} \overline{\hat{p}^{(n)}(\boldsymbol{x}, \omega)\hat{p}^{(m)*}(\boldsymbol{x}, \omega)} \approx \sum_{n} \overline{\hat{p}^{(n)}(\boldsymbol{x}, \omega)\hat{p}^{(n)*}(\boldsymbol{x}, \omega)} \\ &\approx \sum_{n} \overline{\hat{p}^{(n)}_{e_{4j}}(\boldsymbol{x}, \omega)\hat{p}^{(n)*}_{e_{4j}}(\boldsymbol{x}, \omega)} + \sum_{n} \overline{\hat{p}^{(n)}_{\nabla_j \widetilde{v}_i}(\boldsymbol{x}, \omega)\hat{p}^{(n)*}_{\nabla_j \widetilde{v}_i}(\boldsymbol{x}, \omega)} \\ &\quad + \sum_{n} \overline{\hat{p}^{(n)}_{e_{ij}}(\boldsymbol{x}, \omega)\hat{p}^{(n)*}_{e_{ij}}(\boldsymbol{x}, \omega)} = \sum_{n} \overline{\hat{p}^{(n)}_{e_{4j}}(\boldsymbol{x}, \omega)\hat{p}^{(n)*}_{e_{4j}}(\boldsymbol{x}, \omega)} \\ &\quad + \sum_{n} \overline{\hat{p}^{(n)}_{\nabla_j \widetilde{v}_i}(\boldsymbol{x}, \omega)\hat{p}^{(n)*}_{\nabla_j \widetilde{v}_i}(\boldsymbol{x}, \omega)} + \sum_{n} \overline{\hat{p}^{(n)}_{e_{11}}(\boldsymbol{x}, \omega)\hat{p}^{(n)*}_{e_{11}}(\boldsymbol{x}, \omega)} \\ &\quad + \sum_{n} \overline{\hat{p}^{(n)}_{e_{12}}(\boldsymbol{x}, \omega)\hat{p}^{(n)*}_{e_{12}}(\boldsymbol{x}, \omega)} + \sum_{n} \overline{\hat{p}^{(n)}_{e_{21}}(\boldsymbol{x}, \omega)\hat{p}^{(n)*}_{e_{21}}(\boldsymbol{x}, \omega)} + \cdots . \end{aligned} \tag{2.18}$$

The former property can be referred to as mutual orthogonality of the individual source components with respect to the far-field sound power. It should be noted that it does not only require symmetry of the autocorrelation source tensor but also orthogonality of the source modes for the far-field noise solution, which was also previously discussed in the jet noise literature (Goldstein & Leib 2016). In § 4, it will be demonstrated how both of these conditions are satisfied for the SILOET jet case.

Besides, if the density distribution of any particular source component corresponding to a given stress term needs to be analysed in the jet volume, this can also be achieved by noting, for example, that

$$\begin{aligned} P^{(n)}_{e_{ij}} &= \overline{\hat{p}^{(n)}_{e_{ij}}(\boldsymbol{x}, \omega)\hat{p}^{(n)*}_{e_{ij}}(\boldsymbol{x}, \omega)} \\ &= \overline{\left(\int_{V_y} \hat{e}''^{(n)}_{ij}(\boldsymbol{y_\eta}, \omega) \nabla_i \hat{u}^{a(n)}_j(\boldsymbol{y_\eta}, \omega|\boldsymbol{x}) \int_{V_{y1}} \hat{e}''^{*(n)}_{ij}(\boldsymbol{y_{\eta 1}}, \omega) \nabla_i \hat{u}^{a*(n)}_j(\boldsymbol{y_{\eta 1}}, \omega|\boldsymbol{x}) \, \mathrm{d}\boldsymbol{y_{\eta 1}} \, \mathrm{d}\boldsymbol{y_\eta} \right)} \\ &= \int_{V_y} \widetilde{P}^{(n)}_{e_{ij}}(\boldsymbol{y_\eta}) \, \mathrm{d}\boldsymbol{y_\eta}, \end{aligned} \tag{2.19}$$

where $\widetilde{P}^{(n)}_{e_{ij}}(\boldsymbol{y_\eta})$ is the corresponding source density function, given by

$$\widetilde{P}^{(n)}_{e_{ij}}(\boldsymbol{y_\eta}) = \nabla_i \hat{u}^{a(n)}_j(\boldsymbol{y_\eta}, \omega|\boldsymbol{x}) \overline{\hat{e}''^{(n)}_{ij}(\boldsymbol{y_\eta}, \omega) \left(\int_{V_{y1}} \hat{e}''^{*(n)}_{ij}(\boldsymbol{y_{\eta 1}}, \omega) \nabla_i \hat{u}^{a*(n)}_j(\boldsymbol{y_{\eta 1}}, \omega|\boldsymbol{x}) \, \mathrm{d}\boldsymbol{y_{\eta 1}} \right)}. \tag{2.20}$$

It should be noted also that although, inside the integral, (2.20) implicitly includes the fourth rank autocovariance tensor, $\hat{R}^{(n)}_{ijij}(\boldsymbol{y_\eta}, \boldsymbol{y_{\eta 1}}, \omega) = \overline{\hat{e}''^{(n)}_{ij}(\boldsymbol{y_\eta}, \omega)\hat{e}''^{*(n)}_{ij}(\boldsymbol{y_{\eta 1}}, \omega)}$, the

Nozzle diameter, D_j	Contraction ratio	Acoustic Mach number, U_j/c_∞	Reynolds number, U_jD_j/ν	Temperature ratio, T_j/T_∞
0.1016	2.56	0.875	2×10^6	1

TABLE 2. Parameters of the Rolls-Royce SILOET jet case.

latter expensive function does not need to be recorded. Indeed, the computation of the effective source density, $\widetilde{P}^{(n)}_{e_{ij}}(\boldsymbol{y})$, only requires the storage of several realisations of turbulent stresses $\hat{e}''^{(n)}_{ij}(\boldsymbol{y}_{\boldsymbol{\eta}}, \omega)$ and the vector adjoint Green's function $\nabla_i \hat{u}^a_j(\boldsymbol{y}_{\boldsymbol{\eta}}, \omega|\boldsymbol{x})$ for azimuthal modes and frequencies of interest as outlined in § 3.2. The effective source density $\widetilde{P}^{(n)}_{e_{ij}}(\boldsymbol{y})$ can then be reconstructed in the entire 3D jet volume as follows: (i) calculate the inner integral $\int_{V_{y1}} \hat{e}''^{*(n)}_{ij}(\boldsymbol{y}_{\boldsymbol{\eta 1}}, \omega)\nabla_i \hat{u}^{*a}_j(\boldsymbol{y}_{\boldsymbol{\eta 1}}, \omega|\boldsymbol{x})\,\mathrm{d}\boldsymbol{y}_{\boldsymbol{\eta 1}}$ for each realisation of the stress field, (ii) multiply the result by all possible realisation values of the stress field $\hat{e}''^{(n)}_{ij}(\boldsymbol{y}_{\boldsymbol{\eta}}, \omega)$ and (iii) ensemble average over the combined number of realisations and multiply by the Green's function, $\nabla_i \hat{u}^{a(n)}_j(\boldsymbol{y}_{\boldsymbol{\eta}}, \omega|\boldsymbol{x})$.

3. Validation for the SILOET experiment data

3.1. *Jet case definition and flow solution validation*

For validation of the new volume integral method developed, jet conditions from the Rolls-Royce Strategic Investment in Low-carbon Engine Technology (SILOET) experiment performed in the Noise Test Facility (NTF) of QinetiQ are considered (SILOET Programme Rolls-Royce private data). The conditions correspond to a high-speed single-stream subsonic isothermal jet flow issuing from a convergent profiled nozzle. Details of the jet case are summarised in table 2. Two conditions are considered: a zero coflow (the static jet case) and a coflow velocity U_c in the jet streamwise direction corresponding to $M_c = 0.3$, where $M_c = U_c/c_\infty$.

The flow solutions have been obtained with the MILES CABARET solver (Faranosov *et al.* 2013; Semiletov & Karabasov 2013, 2014*b*,*a*) on a hexahedral cylindrical grid of circa 21×10^6 cells in total. For unsteady flow modelling, the governing Navier–Stokes equations are solved in the framework of the monotonically integrated LES (MILES) method (Fureby & Grinstein 2002). The MILES implementation used is based on the low-dissipative and low-dispersive CABARET method (Goloviznin & Samarskii 1998; Karabasov & Goloviznin 2009; Chintagunta, Naghibi & Karabasov 2018) on a hexahedral cylindrical grid of circa 21×10^6 cells in total. Numerical simulations have been performed over approximately 560 time units (TUs), which includes approximately 200 TUs of the initial solution spin-out time. Here, one TU corresponds to the time required for an eddy to travel over one jet diameter, $\mathrm{TU} = D_j/U_j$.

The computational domain is covered with a cylindrical-type computational grid with a Cartesian bloc along the centreline. The grid includes the jet flow downstream of the nozzle exit and spans over approximately 100 jet diameters axially and 30 jet diameters radially. For open boundaries, a combination of characteristic non-reflecting boundary conditions and grid stretching is used to minimise spurious reflections. The standard no-slip adiabatic boundary condition is applied on the nozzle walls. Upstream of the nozzle exit, the computational domain includes part of the nozzle and spreads over five jet diameters.

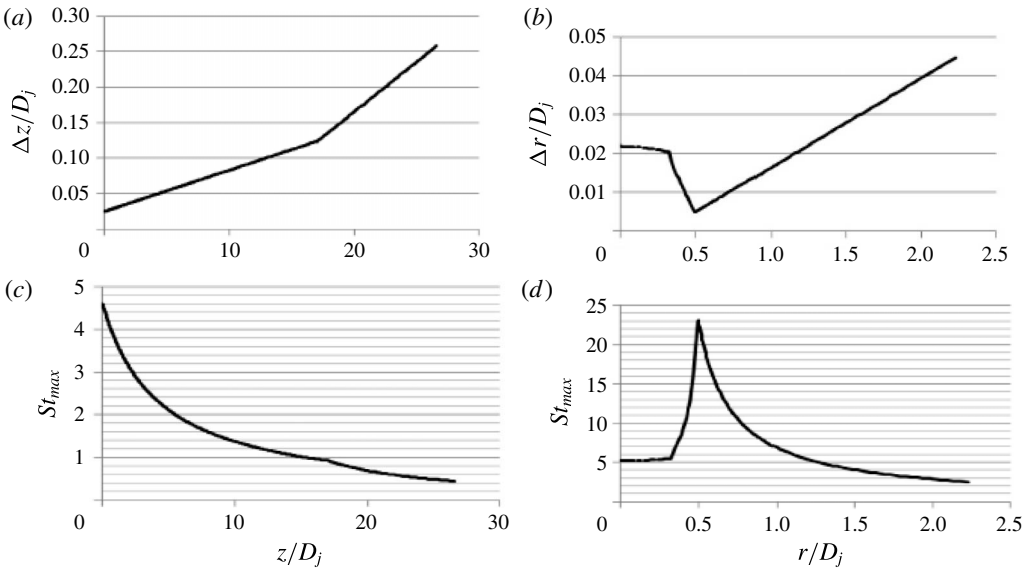

FIGURE 2. Cell size distribution in the axial and radial directions, (*a*) and (*b*), and the corresponding highest resolved acoustic frequencies, (*c*) and (*d*).

Most of the grid cells are clustered in the shear-layer region which is the most important zone for noise generation. Figure 2 shows details of the grid spacing distribution along the jet lipline and radially. The grid has a sufficient resolution for acoustic wave propagation up to $St \sim 1$–2 over the first 8–15 jet diameters from the nozzle exit, where $St = fD_j/U_j$ is the Strouhal number defined by the nozzle diameter.

At the nozzle lip, the grid cell sizes in the radial, streamwise and azimuthal directions are $\Delta r = 0.005D_j$, $\Delta z = 0.025D_j$, $r\Delta\theta = 0.0245D_j$ respectively. This resolution is likely to be too coarse to capture the boundary layer at the nozzle exit and, while no boundary layer modelling was attempted since there are no flow measurements available inside the nozzle from the experiment, this resulted in an initially laminar jet condition in the LES solution. It should be noted that use of the laminar jet inflow condition not only relies on the fast transition of the flow solution to turbulence in accordance with the shear-layer instability development downstream of the nozzle exit but also ignores the fact that the jet flow at such a high Reynolds number is always turbulent at the nozzle exit. Hence, the current idealised treatment of the jet inflow conditions makes the jet development dependent on the numerical method details, which may not be ideal according to the existing jet noise literature (Bogey, Marsden & Bailly 2012; Bres *et al.* 2015). A subject of future work will be to obtain a more accurate LES solution for the same jet case with account for a realistic turbulent jet inflow condition, for example based on the wall-modelled LES approach (Bres *et al.* 2015). In the meantime, it should be pointed out that similar idealised laminar inflow jet conditions were used in other publications on isolated jets (Bres *et al.* 2012; Ingraham & Bridges 2017; Leib, Ingraham & Bridges 2017) without reporting any drastic effect of the initially laminar condition on the downstream jet flow development that defines the far-field noise spectra and acoustic sensitive jet flow properties such as the fourth-order velocity autocorrelation functions. Most recently, Markesteijn & Karabasov (2018) used the MILES CABARET method for computing NASA jets corresponding to set point 7 and 3 conditions at Reynolds numbers of

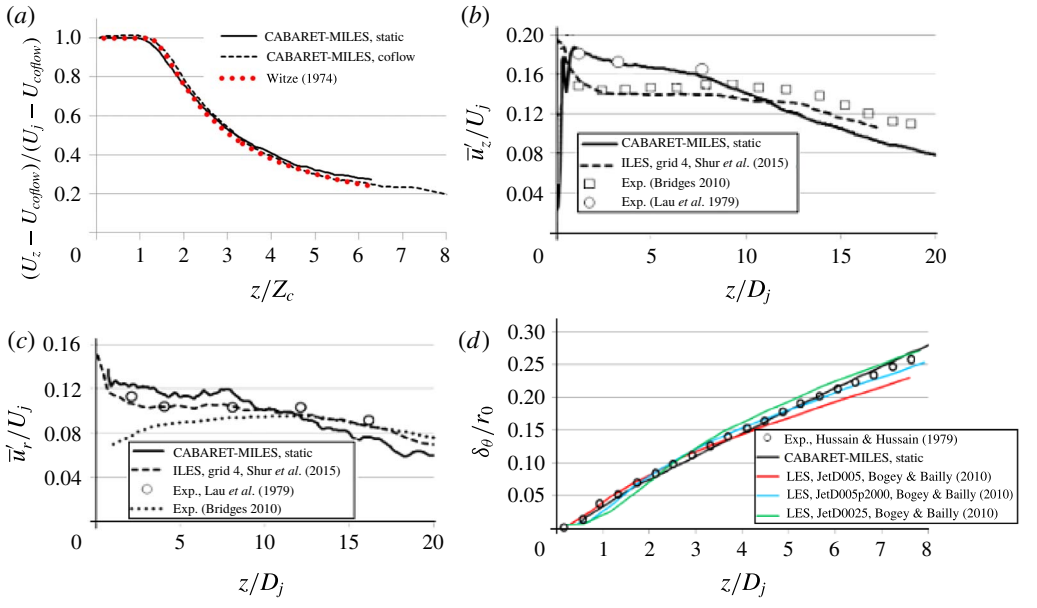

FIGURE 3. (Colour online) Comparison of the CABARET SILOET flow solution with the experimental and computational data available: centreline mean-flow velocity profile (*a*), lipline profile of the axial velocity fluctuation (*b*), lipline profile of the radial velocity fluctuation (*c*) and streamwise profile of the shear-layer thickness (*d*).

around 10^6 on graphics processing units (GPUs) to reduce the LES run time. The GPU LES solutions obtained with the imposition of a laminar inflow jet condition were compared with the solutions obtained by introducing a numerical turbulence grid upstream of the nozzle exit to capture the same velocity fluctuations at the nozzle exit as reported in the NASA experiment. In both cases, with and without imposing the initial disturbances at the nozzle exit, the obtained LES solutions showed similar good agreement with the experiment in predicting the rest of the flow field and the far-field noise spectra.

Figure 3 shows the results of the validation of the presented CABARET SILOET flow solutions in comparison with the experimental data available in the literature.

Figure 3(*a*) compares the centreline profile of the axial mean-flow velocity component with the function $(\overline{v}_z/U_j) = 1 - e^{\alpha/(1-z/Z_0)}$, where Z_0 is the potential core length of the jet and $\alpha = 1.43$ is the Witze empirical parameter, which describes a similitude jet profile, as commonly accepted in high-speed jet flow experiments (Witze 1974).

Figures 3(*b*) and 3(*c*) compare the current LES solutions for jet lipline distributions of the streamwise and transverse velocity component fluctuations with the experimental data from Lau, Morris & Fisher (1979), Bridges & Wernet (2003) and Bridges (2010) as well as with the implicit LES solution obtained on a similar resolution grid ($\sim 20 \times 10^6$ grid cells) from Shur *et al.* (2015) which corresponds to jet conditions of the Boeing experiment (Viswanathan 2004).

To further analyse the current SILOET LES solution in the noise sensitive shear-layer region, following Bogey & Bailly (2010), the streamwise profile of the shear-

layer momentum thickness

$$\delta_\theta = \int_0^{r_{0.04}} \frac{\overline{v}_z}{\overline{U}_c}\left(1 - \frac{\overline{v}_z}{\overline{U}_c}\right) \mathrm{d}r \tag{3.1}$$

is considered, where $\overline{v}_z$ is the local axial mean-flow velocity, $\overline{U}_c$ is the corresponding axial velocity value at the jet centreline and $r_{0.04}$ is defined so that $\overline{v}_z(r_{0.04}) = 0.04\overline{U}_c$.

Figure 3(*d*) compares the above quantity computed from the present LES solution with the experimental data available from Hussein, Capp & George (1994). In addition, LES solutions from several references digitised from Bogey & Bailly (2010) are shown on the same plot. In the latter case, these solutions correspond to various shear-layer resolutions at the nozzle exit ($r/D_j = 0.005$ and 0.0025, denoted by JetD005 and JetD0025 respectively) and with and without additional boundary layer tripping inside the pipe nozzle (JetD005p2000 and JetD005 respectively). In each case, the normalisation based on the jet radius at the nozzle exit $r_0 = D_j/2$ is applied.

Notably, in all cases, the present CABARET SILOET simulation is in good agreement with the referenced experimental and computational data.

To conclude the LES validation section, the turbulent velocity spectra from the current jet flow solution for a few representative points in the shear layer are extracted and their slope is compared with the $-5/3$ that is representative of the inertial range of turbulence cascade in accordance with Kolmogorov's theory (Pope 2000). Because of the limited length of time history available from the LES solution, the spectra are calculated in accordance with the standard signal postprocessing method (Welch 1967) to improve the statistical convergence. Again, the original signal is divided into several subsample signals with 50 % overlap. Each subsample signal is Fourier-transformed with a Hanning window applied and the final spectra are obtained by averaging over all sections. This is the same signal postprocessing technique as is used in the implementation of the volume integral method outlined in §§ 2.2 and 2.3. The results are presented in figure 4, which shows that the current LES solution captures the $-5/3$ slope over at least one octave of the turbulent velocity spectra, as expected from a high-Reynolds-number flow.

At this point, it may be concluded that the laminar inflow jet condition approximation used for the current LES solution did not lead to a significant change in the jet flow dynamics downstream of the nozzle exit in comparison with the existing literature. Therefore, despite the approximation made, the quality of the current LES flow solution is reasonable in terms of its further input in the acoustic analogy modelling that is the core part of the current publication.

3.2. *Far-field noise spectra predictions and comparison with the Ffowcs Williams–Hawkings method*

Having selected a sufficiently large cylindrical part of the computational domain (25 D_j axially times 2 D_j radially) downstream of the nozzle exit, all components of the generalised fluctuating turbulent stresses $e''_{\mu j}$ are extracted from the LES solution and decomposed into 10 azimuthal modes and 50 frequencies within $0.05 < St < 3$. The resulting stress fields are substituted in the volume integral formulation of the generalised acoustic analogy (2.12), (2.14) to compute the far-field noise spectra and compare the results with the far-field microscope measurements from the SILOET experiment. The far-field microphone data correspond to a distance of 120 D_j from the centre of the nozzle exit.

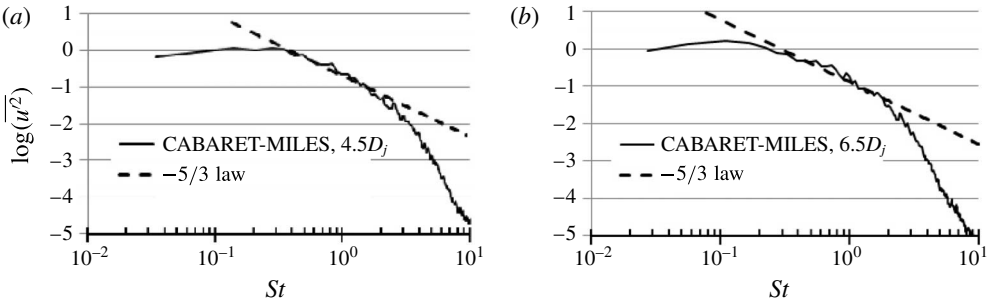

FIGURE 4. CABARET SILOET results for the turbulent velocity spectra at two representative jet lipline locations.

For statistical averaging of the fluctuating stress signals obtained from LES, 20 subintervals with 50 % overlap are used. The computational cost of the volume integral solution is mainly due to computation of the integral sums for the multiple realisations of the LES stress fields required, since the computation of the semianalytical Green's function is extremely fast. The total cost of applying the volume integral method to calculate the far-field noise is a small fraction of the computational cost of the LES solution (∼20 min on a workstation compared with a few weeks on a large computer cluster with hundreds of parallel processes respectively).

In terms of computer memory, the major cost of the volume integral method is due to the recording of the various realisations of the 12 generalised stress components in the 3D jet volume. However, since the stresses only need to be recorded for a discrete number of frequencies, while the Fourier transformation is performed during the simulation run, and the flow solution is required for a limited number of azimuthal modes, the total cost is only marginally larger compared with that of standard 3D surface integral methods.

To cross-verify the far-field noise predictions of the volume integral formulation of the Goldstein generalised acoustic analogy, the same LES solution is applied in the framework of the penetrable formulation of the Ffowcs Williams–Hawkings (FW–H) surface integral method. The method is based on computing the acoustic integrands corresponding to the 'thickness' and 'dipole' terms on a control surface that confines the jet with all important noise sources (di Francescantonio 1997; Brentner & Farassat 1998) and propagating the solution to the far field using the analytical free-space Green's function. Under the assumption that all significant noise sources are included inside the control surface, the external quadrupole sources are ignored. Following Shur *et al.* (2015), a sufficient number of closing discs (∼10) at approximately 25 jet diameters downstream of the nozzle exit are used. An average far-field prediction of the results obtained with the same conical-shaped control surface with different closing discs (figure 5) was used to filter out the pseudosound effect due to vorticity waves crossing the control surface. Upstream of the nozzle exit, the control surface confines the nozzle lip and is left open. Furthermore, since the solution of the penetrable formulation of the FW–H method is known to be sensitive to the location of the integration surface, several (denoted as 'sets' in figure 5) were considered before the optimum one (set no. 2) was selected to make sure that the acoustic integration surface was located within the region of a sufficient grid resolution while sufficiently far away from the vorticity-rich zones. To process the time signal at the far-field microphone location, the same signal processing method

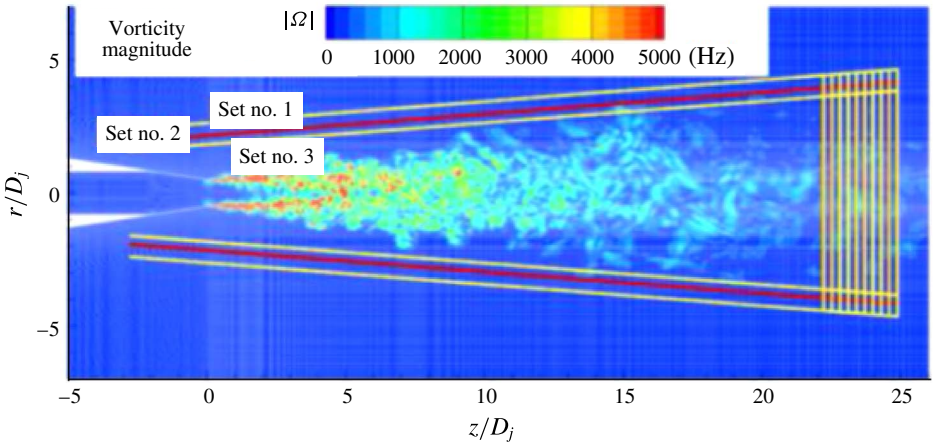

FIGURE 5. (Colour online) Location of integration surfaces used with the Ffowcs Williams–Hawkings method relative to a typical distribution of the instantaneous vorticity magnitude in the SILOET jet.

based on a Fourier transform with subsample averaging (Welch 1967) was applied as in the volume integral method based on the acoustic analogy.

Figure 6 compares the sound power spectral density (PSD) obtained with the Goldstein generalised acoustic analogy implementation (2.12), (2.14) and with those of the FW–H method. Both predictions are within 2–3 dB of the experiment from $St \sim 0.1$–0.2 to $St \sim 2$–3 for polar angles 30°–90° to the jet axis.

It should be noted that, for the 30° angle to the jet, frequencies lower than $St \sim 0.2$ are attenuated for both the FW–H and the acoustic analogy solution (resulting in a ∼4 dB error with respect to the experiment). This attenuation is probably due to the insufficient LES grid resolution at the end of the potential core of the SILOET jet. This is also in accordance with the results of Markesteijn & Karabasov (2018), who examined the grid sensitivity of the MILES CABARET solutions with the FW–H method on several LES grids of circa 60–80×10^6 cells with various refinements for similar high-speed jet cases. Besides, for the same 30° angle to the jet flow, the acoustic analogy solution appears to be less accurate in the medium-frequency range, $0.2 < St < 0.4$, in comparison with the FW–H prediction which is virtually 'spot on' for a 30° angle, e.g. remains within 0.5–1 dB accuracy with respect to the experiment for $0.2 < St < 1.5$. One explanation for the discrepancy could be the simplified locally parallel flow approximation that was applied for solving the sound mean-flow propagation problem in the current acoustic analogy implementation. Hence, future work will be devoted to implementing a more sophisticated evolving mean-flow propagation model within the suggested volume integral approach. For example, further steps may involve a numerical solution of the adjoint linearised Euler equations for the fully evolving jet flow following the method of Karabasov & Hynes (2006), and using non-parallel flow asymptotics within the semianalytical approach suggested by Afsar *et al.* (2017). On the other hand, it should also be recalled that, in comparison with the FW–H solution, there is no single calibration parameter involved in defining the integration domain of the acoustic analogy method. Hence, the current predictions of the acoustic analogy method were not at all 'calibrated' compared with the FW–H solution based on the optimal control integration surface.

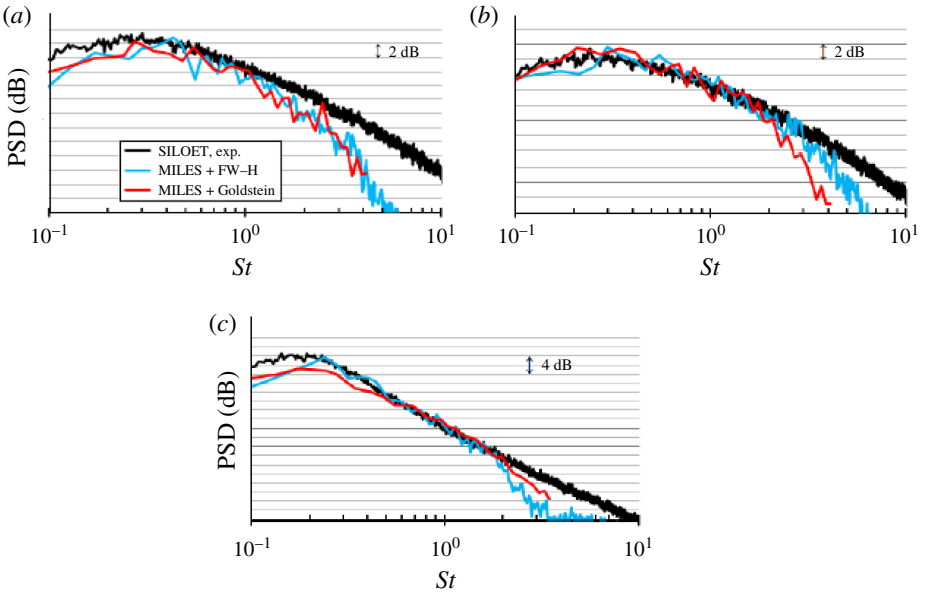

FIGURE 6. (Colour online) Validation of the far-field noise spectra predictions of the volume integral acoustic analogy method in comparison with the experiment and the reference FW–H solution for the isothermal static SILOET jet: 90° polar angle (*a*), 60° polar angle (*b*), 90° and 30° (*c*) polar angle to the jet flow.

This means that the 0.5–1 dB accuracy achieved with the FW–H method for the 30° angle noise spectrum predictions on the current 21 million LES grid could be slightly fortuitous and future work should also involve improving the LES grid resolution for the current jet case.

To demonstrate the importance of the absence of calibration parameters for jet noise predictions, the second SILOET jet case, which corresponds to a coflow in the jet streamwise direction at $M_c = 0.3$, is considered. Similarly to the static jet case, the CABARET solution is first obtained for the SILOET jet flow case taking the coflow effect into account. The LES solution is then applied for the volume integral formulation as well as for the penetrable FW–H formulation without any additional calibration of either of the acoustic modelling methods. For the FW–H method, this means using the same acoustic control surface in the coflow case as in the previous static jet case.

Figure 7 compares the sound spectra predictions by both methods and with the experiment for 90° observer location. There is a strong amplification of the FW–H solution notable at low frequencies, which is a manifestation of spurious pseudosound waves that were not sufficiently abated in this case. It should be noted that there are recipes in the FW–H literature (e.g. Shur *et al.* 2005) regarding how to adjust the acoustic surface location depending on the jet operating conditions to filter out the pseudosound effects, but these recipes are empirical in nature. In comparison with these, the noise spectra predictions of the current volume integral method based on the acoustic analogy are within 2–3 dB of the experiment for both the static and the coflow jet conditions without any empirical calibration needed.

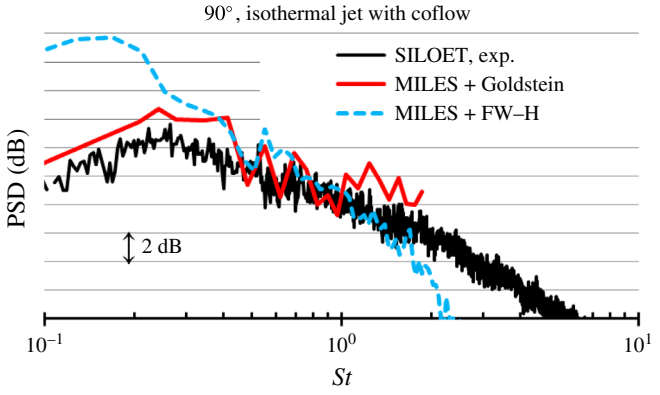

FIGURE 7. (Colour online) Far-field noise spectra of the isothermal SILOET jet with the coflow for 90° polar angle: comparison of the volume integral method predictions with those of the FW–H method and with the experiment.

4. Noise generation and propagation mechanisms

Having validated the volume integral method for far-field noise spectra prediction in the previous section, here we will use it to analyse the contributions of individual sound generation and propagation components of the Goldstein generalised acoustic analogy model for the static SILOET jet.

4.1. *Contribution of the source volume to the far-field noise*

Figure 8 shows the far-field spectra predictions based on various subdomains of the original integration volume for 90° microphone angle. Each of the small parts of the original control volume has a cylindrical shape and starts at the nozzle exit. The radius and the streamwise extent of the control volume are varied one at a time. The change of the far-field sound spectra due to decrease of the integration domain in the streamwise direction down to the cylindrical volume $(2 \times 4)D_j$ (radially times axially) is demonstrated in figure 8(*a*), and the same for the radial direction down to $(0.75 \times 25)D_j$ (radially times axially) is shown in figure 8(*b*). In both cases, as the size of the source volume decreases, the low frequencies become attenuated whereas the frequencies higher than $St \sim 0.4$ remain almost unaffected by the control volume change applied. Furthermore, starting from a certain elongated cylinder shape of the source volume, which is approximately $(1.5 \times 10)D_j$ (radially times axially), that is, approximately a factor of 2 larger than the jet plume dimensions (the potential core length of the SILOET jet is approximately $5.5D_j$), the same relative change of the control volume in the radial or streamwise direction leads to approximately the same noise spectra. For example, the effect of the change of control volume in the radial direction from $1.5D_j$ to $0.75D_j$ on the low part of the frequency spectra is approximately the same as that of the change in the streamwise direction from $15D_j$ to $6D_j$. Results of varying the size of the integration volume for the 30° angle spectra (not shown) demonstrate the same effect. This suggests that the effective source shape, which in terms of the autocovariance of fluctuating turbulent stresses (2.6) corresponds to the source correlation volume, changes approximately in proportion to the jet dimensions. The effective source shrinks for high-frequency sound and the high-frequency sources tend to be more compactly located closer to the nozzle exit and the jet lipline area compared with the low frequencies.

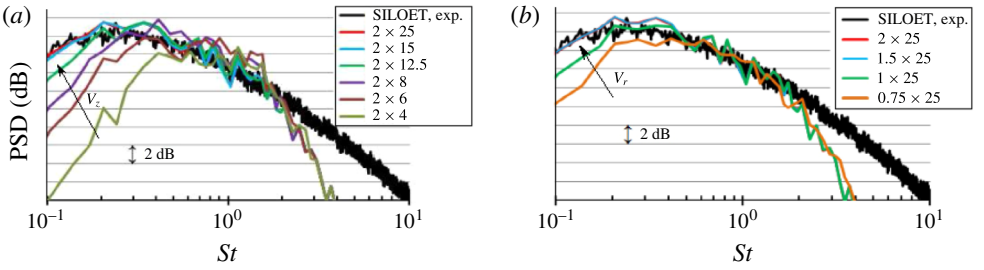

FIGURE 8. (Colour online) Effect of shrinking the cylindrical source integration domain on the far-field noise spectra at 90° observer angle: varying the source volume in the streamwise direction V_z (a) and the radial direction V_r (b).

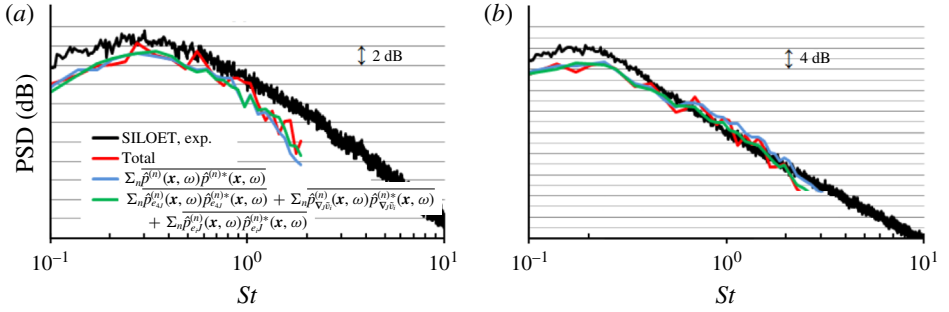

FIGURE 9. (Colour online) Orthogonality of individual source term components for far-field sound spectra at 60° (a) and 30° angle (b) to the jet flow. The predictions shown correspond to the total spectra, the spectra solutions with the assumption of orthogonality of different azimuthal modes of the source, and the assumption of orthogonality of different stress terms.

4.2. *Orthogonality of different source components for far-field power noise spectra*

Figure 9 shows far-field noise spectra predictions for two typical microphone angles based on the complete source integration volume with and without neglecting some of the mixed terms in the acoustic integral to investigate the effect of mutual orthogonality of individual source terms.

The total spectra solution and the reference experimental data are included in the same panels for comparison. The two approximate solutions shown correspond to (i) assuming the orthogonality of different azimuthal modes $\sum_n \overline{\hat{p}^{(n)}(\boldsymbol{x},\omega)\hat{p}^{(n)*}(\boldsymbol{x},\omega)}$ and (ii) further assuming the orthogonality of different source terms $\sum_n \overline{\hat{p}^{(n)}_{e_{4j}}(\boldsymbol{x},\omega)\hat{p}^{(n)*}_{e_{4j}}(\boldsymbol{x},\omega)} + \sum_n \overline{\hat{p}^{(n)}_{\nabla_j \widetilde{v}_i}(\boldsymbol{x},\omega)\hat{p}^{(n)*}_{\nabla_j \widetilde{v}_i}(\boldsymbol{x},\omega)} + \sum_n \overline{\hat{p}^{(n)}_{e_{ij}}(\boldsymbol{x},\omega)\hat{p}^{(n)*}_{e_{ij}}(\boldsymbol{x},\omega)}$ for the far-field sound power spectra in (2.18). It should be noted that both of the approximate solutions are within 1–2 dB of the total spectra for most frequencies, which confirms the validity of the assumption of mutual orthogonality for different stress term components in the SILOET jet case.

4.3. *Effect of the source type and directivity on far-field noise*

Figure 10 shows the contributions to the far-field noise spectra produced by various turbulent fluctuating stresses in comparison with the total spectra. There are

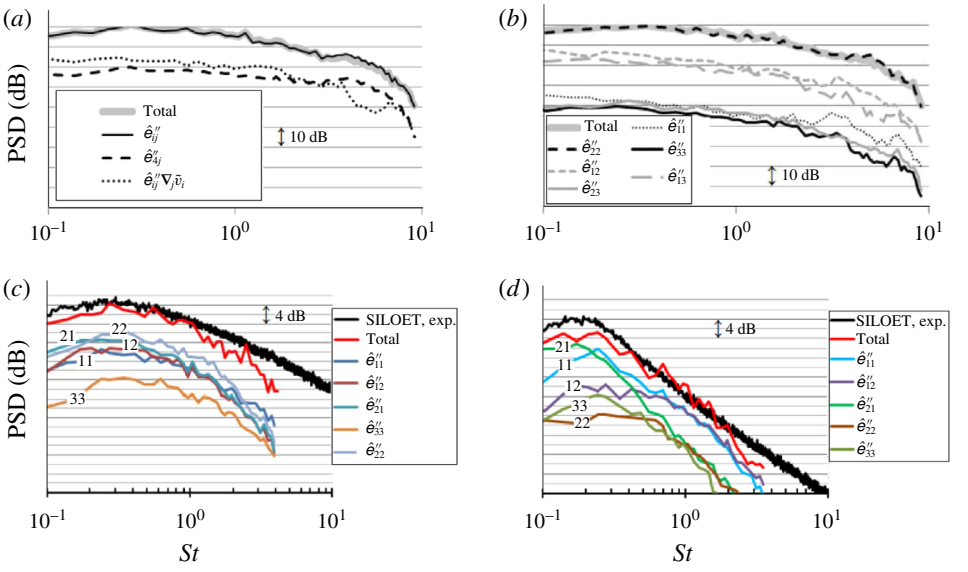

FIGURE 10. (Colour online) Contributions of individual fluctuating stresses to far-field noise spectra: comparison of the fluctuating Reynolds stress term with the fluctuating enthalpy and the velocity divergence terms for 90° polar angle (*a*), comparison of various components of the fluctuating Reynolds stress term for 90° polar angle (*b*), comparison of various components of the fluctuating Reynolds stress term for 60° polar angle (*c*) and comparison of various components of the fluctuating Reynolds stress term for 30° polar angle (*d*).

contributions of various components of the fluctuating Reynolds stresses, e''_{ij}, considered (i, $j = 1, 2, 3$), where $\boldsymbol{e}_1$ is the Cartesian coordinate in the jet flow direction, $(\boldsymbol{e}_2, \boldsymbol{e}_3)$ are in the transverse plane and $(\boldsymbol{e}_1, \boldsymbol{e}_2)$ are in plane with the far-field microphone, as discussed in § 2.2. The contributions of the enthalpy fluctuation term, $\hat{e}''_{4j}(\boldsymbol{y}, \omega)$, and the term that includes the velocity divergence, $\hat{e}''_{ij}(\boldsymbol{y}, \omega)\nabla_j \widetilde{v}_i(\boldsymbol{y})$, are also shown. The integration domain corresponds to the entire jet source volume.

Figure 10(*a*) shows that for 90° microphone angle, the contribution of the enthalpy term and the velocity divergence term to the far-field noise is negligible compared with the fluctuating Reynolds stresses. This is the generalised stress term which corresponds to the Lighthill quadrupole noise source. Fluctuating Reynolds stresses remain the dominant noise component terms for other polar angles as well. However, the directivity of the dominant Reynolds stress component changes depending on the polar angle. For example, the e''_{22} stress component is most important at 90° angle, $\hat{e}''_{22}$, $\hat{e}''_{21}$, $\hat{e}''_{12}$, $\hat{e}''_{11}$ all become significant for 60°, and $\hat{e}''_{11}$, $\hat{e}''_{12}$, $\hat{e}''_{21}$ are important for 30°. The relative contribution of the Reynolds stress components also depends on the sound frequency. For example, the relative importance of e''_{12} increases at high frequencies, while e''_{21} is most important at low frequencies and small angles to the jet flows. The contribution of the out-of-plane components remains negligible for all angles and frequencies.

4.4. *Contribution of the azimuthal source modes to the far-field noise*

Figure 11 shows the contributions of different modes of the fluctuating Reynolds stresses to the far-field noise spectra for different polar angles. The total spectra

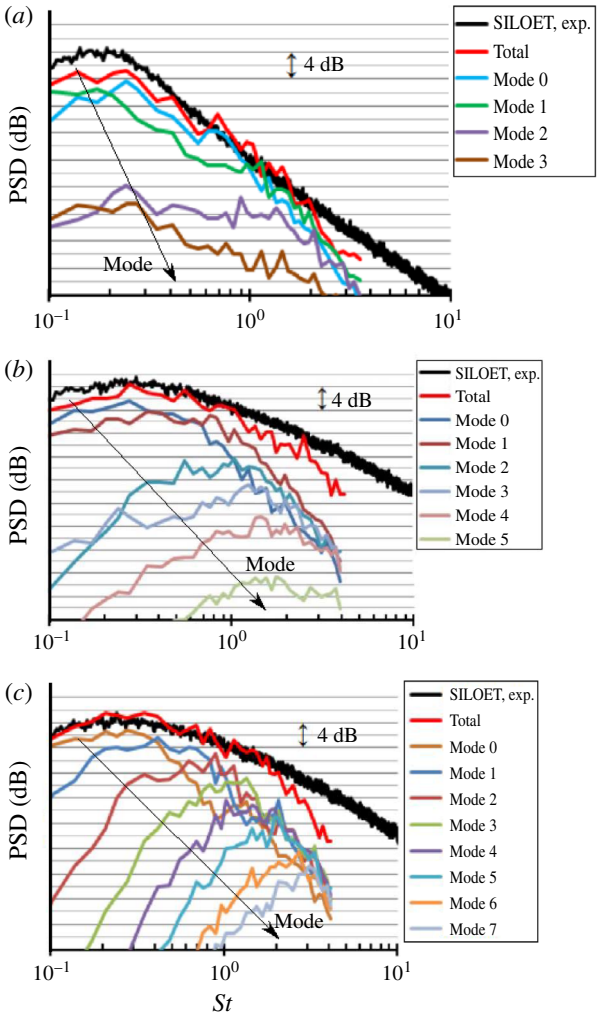

FIGURE 11. (Colour online) Contributions to the far-field noise spectra from different azimuthal modes of the fluctuating Reynolds stresses for 30° (*a*), 60° (*b*) and 90° (*c*) polar angle to the jet flow.

solutions based on the same complete integration volume and the experimental data are shown on the same plots for comparison.

For the 30° angle to the jet flow, the axisymmetric azimuthal mode, $n = 0$, is the most dominant component in the frequency range $0.2 < St < 0.8$, where $St \sim 0.2$ corresponds to the lowest numerical frequencies, which are numerically captured for sound spectra predictions at this polar angle (see the discussion in § 3). This observation is in agreement with existing experiments Cavalieri *et al.* (2013), which show that it is the zero-order azimuthal mode, $n = 0$, that mostly contributes to jet noise at the 30° polar angle.

For high polar angles, 60° and 90° to the jet flow, the first asymmetric azimuthal mode, $n = 1$, becomes increasingly important starting from mid frequencies, $St \geqslant 0.4$. As the sound frequency increases, the importance of other high-order modes also

increases. The increase in relative importance of high-order modes with frequency is most notable at the 90° polar angle compared with small angles to the jet flow. For example, at $St = 1$ and 30° polar angle, there are only a few significant modes, $n = 0$ and 1, that contribute to the far-field noise spectra efficiently, while for the 60° polar angle, it is the $n = 1$ mode that is most significant, and for the 90° angle, it is the modes $n = 1$ and 2 that contribute to the far-field noise effectively. All of this is also consistent with the analysis presented in Goldstein (1975) and Goldstein *et al.* (2012), who showed that the $n = 0$ mode is highly directional, and hence does not significantly contribute to the 90° noise spectrum. Notably, the effect of high-order azimuthal modes on sound spectra at large polar angles to the jet flow, which is captured by the current calibration-free implementation of the generalised acoustic analogy, would be difficult to reproduce by approaches based on modelling of coherent large-scale structures that stem from the instability wave theory.

4.5. *Effect of the mean-flow sound propagation on the far-field noise*

In addition to the effect of the source integration volume and individual source components, the effect of mean-flow sound propagation is an important contributor to the far-field noise. In this subsection, the effect of the Green's function on the far-field solution is analysed by comparing the noise predictions obtained with the locally parallel solution and those obtained with the free-space solution which completely ignores the jet refraction effect. In each case, the integration volume and the noise source description are fixed to be the same and correspond to a complete set of the fluctuating stresses, $e''_{\mu j}$, of the Goldstein generalised acoustic analogy.

Both noise spectra solutions, with and without taking the mean-flow effect into account, are integrated in the frequency band $0.05 < St < 2$ and compared with the corresponding overall sound pressure level (OASPL) data from the SILOET experiment.

The results are given in table 3, which shows the differences between the reference OASPL data and the two far-field predictions of the volume integral method based on the Goldstein generalised acoustic analogy with and without considering the mean-flow propagation effect as a function of the polar angle. The error for the solution that includes the corresponding Green's function that takes into account the mean-flow effect remains within 0.5–2.2 dB. Compared with this, the error of the same volume integral method based on the free-space Green's function monotonically grows with decrease of the polar angle and reaches 6 dB for 30° microphone angle. It should be noted that the error can be expected to be much larger at the higher Mach numbers corresponding to take-off conditions. This error growth signifies the importance of mean-flow propagation effects for small angles of noise radiation to the jet flow. The latter is in agreement with the existing jet noise literature that discusses the effect of mean-flow sound propagation modelling on noise spectra predictions at small angles to the jet flow (compare with figure 16 from Karabasov *et al.* (2010) and figure 12(*a*,*b*) from Karabasov *et al.* (2013)).

For comparison, the same table also shows the OASPL error, which corresponds to an integral volume implementation of the classical Lighthill acoustic analogy based on the LES solution of a high-speed jet case from Bogey, Bailly & Juve (2001). For this case, there are no experimental data available and the reference 'true solution' was defined by computing the LES solution inside a large control surface and then integrating the latter to the far field using the Kirchhoff method. Using the digitised data from Bogey *et al.* (2001), the Lighthill acoustic analogy error was then specified

	OASPL error at 90° (dB)	OASPL error at 60° (dB)	OASPL error at 30° (dB)
Goldstein acoustic analogy with mean-flow sound propagation modelling	0.5	2	2.2
Goldstein acoustic analogy with no mean-flow sound propagation modelling	0.5	3.2	6
Lighthill acoustic analogy (Bogey *et al.* 2001)	2.5	−5	2.5

TABLE 3. Dependence of the OASPL error on the acoustic model and the polar angle.

as the difference between the reference 'true solution' and the OASPL predictions of the Lighthill acoustic analogy solution. It should be noted that the latter error fluctuates between +2.5 dB and −5 dB and does not show any particular trend with the polar angle.

5. Conclusions

A new volume integral formulation of the Goldstein generalised acoustic analogy has been developed. On one hand, it can be seen as a significant extension of previous volume integral methods in the acoustic analogy literature. On the other hand, the new method can be regarded as a new volume integral implementation of the generalised acoustic analogy, which does not require the calculation and recording of the expensive generalised stress tensor autocovariance function and is automatically extendable to asymmetric jets. It is also shown how the new implementation allows a direct correspondence between the fluctuating stress components in the jet flow and their effect on the far-field noise power spectra. Thanks to these properties, the new volume integral method can fully utilise the availability of time-dependent three-dimensional LES flow solutions to investigate jet noise mechanisms at a new level of detail compared with state-of-the-art experimental or theoretical studies. Examples of the modelling are provided for a particular choice of the LES method, an isothermal subsonic jet, and jet inflow conditions, but the general approach developed is suitable for any DNS, LES or hybrid LES–RANS technique, and jet flow of the user's choice. For example, the suggested volume integral method is sufficiently robust and requires only minor modifications for supersonic jet noise predictions, where an application of the critical layer correction in the locally parallel Green's function solution would be required (Goldstein & Leib 2008).

For validation of the new volume integral formulation, the high-speed subsonic isothermal static jet case corresponding to the Rolls-Royce SILOET experiment is considered. The SILOET jet flow shares many similarities with other high-speed jets in the literature in terms of both the flow characteristics and the turbulent velocity spectra. The SILOET flow solution is calculated with the MILES CABARET solver. For simplicity of the modelling, an idealised laminar condition is imposed at the nozzle exit; this choice is consistent with the jet noise literature. The validation is performed using the reference experimental and computational data available and also the existing theory of Kolmogorov for turbulent velocity spectra. The far-field noise spectra predictions of the new volume integral method are validated against the

far-field microphone data of the SILOET experiment with 2–3 dB agreement reported for a range of frequencies, $0.1 < St < 2$, and polar angles, 60°–90°, with respect to the jet flow. A similar agreement with experiment is achieved for the same LES data when using the standard penetrable formulation of the FW–H surface integral method.

For a 30° angle to the jet flow and frequencies below $St = 0.2$, both the acoustic analogy and the FW–H solution underpredict the experiment by 4 dB, which is probably due to the insufficient LES grid resolution at the end of the potential core of the jet. For this polar angle, the noise spectrum prediction of the FW–H method appears to be more accurate (0.5–1 dB error) in comparison with the acoustic analogy solution (2–3 dB error). This difference can be explained by the approximate locally parallel Green's function solution used in the current acoustic analogy implementation as well as the opportunistic calibration involved in the selection of the optimal FW–H integration surface. Most importantly, compared with the volume integral method, the predictions of the surface integral method are sensitive to the control surface location, and, furthermore, cannot be used to analyse the jet sources inside the jet.

To demonstrate the capabilities of the new volume integral formulation of the Goldstein generalised acoustic analogy in revealing the salient properties of jet noise, the sound generation and propagation effects of the model are systematically analysed.

First, by truncating the integration volume in the radial and streamwise directions, it is shown that the effective source correlation volume is proportional to the physical jet dimensions. The effective source size tends to reduce with frequency without changing its shape. The high-frequency source region is located more compactly near the nozzle exit and the jet lipline compared with the low-frequency noise sources, which are more distributed, in agreement with existing jet noise experiments (Tam *et al.* 2008).

Then, it is shown that the individual stresses in terms of their modes and components are mutually orthogonal in the far-field spectra: the result of ignoring the mixed terms in the far-field noise spectra is virtually identical to the full noise spectra of the SILOET jet considered. This is in agreement with other publications in the jet noise literature that consider only symmetric terms of the generalised stress tensor autocovariance, $R_{\mu j \mu j}$, to be important for jet noise and ignore the effect of different azimuthal mode coupling for axisymmetric jet flows.

The effect of individual source types, such as the fluctuating Reynolds stress components, the enthalpy fluctuation term and the velocity divergence term, and also that of different azimuthal source modes on the far-field noise spectra is analysed. Here, it is demonstrated that the fluctuating Reynolds stress is the dominant component for all polar angles compared with other source types. This is in agreement with the quadruple noise source behaviour expected in the isothermal jet noise case considered. Furthermore, it is shown how the relative importance of individual Reynolds stresses changes depending on their directivity, the polar angle and the sound frequency. In particular, the most efficient components of the fluctuating Reynolds stresses are always in plane with the observer position. For 90° polar angle, it is just one stress component that is important and that corresponds to the fluctuating stress pointing in the observer direction. For 60° and 30° angles to the jet, important noise sources have multiple directivity and include several longitudinal and transverse stress components. It also shown how the importance of high-order azimuthal modes grows with the sound frequency and the polar angle. In particular, in agreement with experiments (Cavalieri *et al.* 2013), it is shown that it is the zero-order azimuthal mode, $n = 0$, that mostly contributes to jet noise at the 30° polar angle to the jet flow. In comparison with this, the azimuthal modes $n = 1$ and 2 are very important for sound radiation at 90° angle, which is in agreement with the previous analysis

(Goldstein 1975; Goldstein *et al.* 2012). Notably, the effect of the importance of high-order azimuthal modes for sound radiation at large polar angles to the jet flow, which has been captured here, would be difficult to reproduce by other methods such as those based on instability wave modelling of large-scale structures.

Finally, it is demonstrated that the mean-flow propagation plays a key role in the far-field noise for small angles to the jet flow. The explicit account of the mean-flow propagation effects is a distinctive feature of the Goldstein generalised acoustic analogy compared with other acoustic analogy models such as the Lighthill analogy. Compared with the generalised acoustic analogy, the Lighthill model can be prone to serious errors in overall sound pressure levels when implemented with LES that cannot fully resolve the entire range of acoustically important flow scales, including both the turbulence and the mean-flow propagation effects.

As a final remark, it should be recalled that all sound predictions with the current volume integral method have been obtained using the simplified locally parallel flow model for sound propagation. While the incorporation of more complex mean-flow propagation models, which would account for evolving jet effects, will be a subject of future work, the 2–3 dB accuracy of the current noise spectra predictions for most angles and frequencies calls for a revision of some earlier concepts and theories. For example, in a number of works in the literature on the Goldstein generalised acoustic analogy, there was a strong sensitivity of high-speed jet noise predictions to the evolving jet effects reported; hence, a high importance of these effects for jet noise predictions was concluded. However, all of these models were based on modelling the fluctuating stress autocovariance function in seven-dimensional space–time and using some approximations for a convolution product of the source function with the Green's function to obtain the final noise spectra. Hence, there occurs a possibility that it was actually the exaggerated sensitivity of these models to the source model calibration parameters rather than details of the jet flow evolution that was the real reason behind the previous conclusions. This calls for a new investigation of the importance of evolving jet effects for far-field noise spectra predictions based on the suggested calibration-free volume integral approach.

Acknowledgements

The work has been partially supported by the UK Engineering and Physical Sciences Research Council (EP/I017747/1) and partially by the Aero Acoustics Research Consortium (AARC). The authors are grateful to the UK Government for supporting the SILOET programme during which the model-scale data were acquired in the QinetiQ NTF, and Dr P. Strange (Rolls-Royce Plc) for facilitating access to these data. The authors are grateful to Dr A. Markesteijn (GPU-Prime) for valuable discussions.

REFERENCES

AFSAR, M. Z., GOLDSTEIN, M. E. & FAGAN, A. 2011 Enthalpy-flux/momentum-flux coupling in the acoustic spectrum of heated jets. *AIAA J.* **49** (11), 2522–2531.

AFSAR, M. Z., SESCU, A. & LEIB, S. J. 2016 Predictive capability of low frequency jet noise using an asymptotic theory for the adjoint vector Green's function in non-parallel flow. *AIAA Paper* 2016–2804.

AFSAR, M. Z., SESCU, A., SASSANIS, V. & LELE, S. K. 2017 Supersonic jet noise predictions using a unified asymptotic approximation for the adjoint vector Green's function and LES data. In *23rd AIAA/CEAS Aeroacoustics Conference*, *AIAA AVIATION Forum. AIAA Paper* 2017–3030.

BOGEY, C. & BAILLY, C. 2010 Influence of nozzle-exit boundary-layer conditions on the flow and acoustic fields of initially laminar jets. *J. Fluid Mech.* **663**, 507–540.

BOGEY, C., BAILLY, C. & JUVE, D. 2001 Noise computation using Lighthill's equation with inclusion of mean flow–acoustic interactions. *AIAA Paper* 2001-2255.

BOGEY, C., MARSDEN, O. & BAILLY, C. 2012 Influence of initial turbulence level on the flow and sound fields of a subsonic jet at a diameter-based Reynolds number of 10^5. *J. Fluid Mech.* **701**, 352–385.

BRENTNER, K. S. & FARASSAT, F. 1998 Analytical comparison of the acoustic analogy and Kirchhoff formulation for moving surfaces. *AIAA J.* **36** (8), 1379–1386.

BRES, G. A., JAUNET, V., LE RALLIC, M., JORDAN, P., COLONIUS, T. & LELE, S. K. 2015 LES for jet noise: the importance of getting the boundary layer right. *AIAA Paper* 2015-2535.

BRES, G. A., NICHOLS, J. A., LELE, S. K., HAM, F. E., SCHLINKER, R. H., REBA, R. A. & SIMONICH, J. C. 2012 Unstructured large eddy simulation of a hot supersonic over-expanded jet with chevrons. In *18th AIAA/CEAS Aeroacoustics Conference, 33rd AIAA Aeroacoustics Conference*. *AIAA Paper* 2012-2213.

BRIDGES, J. 2010 Establishing consensus turbulence statistics for hot subsonic jets. *AIAA Paper* 2010-3751.

BRIDGES, J. & WERNET, M. 2003 Measurements of aeroacoustic sound sources in turbulent jets. *AIAA Paper* 2003-3130.

CAVALIERI, A. V. G., RODRIGUEZ, D., JORDAN, P., COLONIUS, T. & GERVAIS, Y. 2013 Wavepackets in the velocity field of turbulent jets. *J. Fluid Mech.* **730**, 559–592.

CHINTAGUNTA, A., NAGHIBI, S. E. & KARABASOV, S. A. 2018 Flux-corrected dispersion-improved CABARET schemes for linear and nonlinear wave propagation problems. *Comput. Fluids* **169**, 111–128.

CURLE, N. 1955 The influence of solid boundaries upon aerodynamic sound. *Proc. R. Soc. Lond.* A **231** (1187), 505–514.

DEPURU MOHAN, N. K., DOWLING, A. P., KARABASOV, S. A., XIA, H., GRAHAM, O., HYNES, T. P. & TUCKER, P. G. 2015 Acoustic sources and far-field noise of chevron and round jets. *AIAA J.* **53** (9), 2421–2436.

FARANOSOV, G. A., GOLOVIZNIN, V. M., KARABASOV, S. A., KONDAKOV, V. G., KOPIEV, V. F. & ZAITSEV, M. A. 2013 CABARET method on unstructured hexahedral grids for jet noise computation. *Comput. Fluids* **88**, 165–179.

FFOWCS WILLIAMS, J. E. 1963 The noise from turbulence convected at high speed. *Phil. Trans. R. Soc. Lond.* **255**, 469–503.

FFOWCS WILLIAMS, J. E. & HAWKINGS, D. L. 1969 Sound generation by turbulence and surfaces in arbitrary motion. *Phil. Trans. R. Soc. Lond.* A **264**, 32142.

DI FRANCESCANTONIO, P. 1997 A new boundary integral formulation for the prediction of sound radiation. *J. Sound Vib.* **202** (4), 491–509.

FREUND, J. B. 2003 Noise-source turbulence statistics and the noise from a Mach 0.9 jet. *Phys. Fluids* **15** (6), 1788–1799.

FUREBY, C. & GRINSTEIN, F. F. 2002 Large eddy simulation of high-Reynolds-number free and wall-bounded flows. *J. Comput. Phys.* **181**, 68–97.

GOLDSTEIN, M. E. 1975 The low frequency sound from multipole sources in axisymmetric shear flows, with application to jet noise. *J. Fluid Mech.* **70** (3), 595–604.

GOLDSTEIN, M. E. 2002 A unified approach to some recent developments in jet noise theory. *Intl J. Aeroacoust.* **1** (1), 1–16.

GOLDSTEIN, M. E. 2003 A generalized acoustic analogy. *J. Fluid Mech.* **488**, 315–333.

GOLDSTEIN, M. E. 2010 Relation between the generalized acoustic analogy and Lilley's contributions to aeroacoustics. *Intl J. Aeroacoust.* **9** (4–5), 401–418.

GOLDSTEIN, M. E. 2011 Recent developments in the application of the generalized acoustic analogy to jet noise prediction. *Intl J. Aeroacoust.* **10** (2–3), 89–116.

GOLDSTEIN, M. E. & LEIB, S. J. 2008 The aero-acoustics of slowly diverging supersonic jets. *J. Fluid Mech.* **600**, 291–337.

GOLDSTEIN, M. E. & LEIB, S. J. 2016 Azimuthal source non-compactness and mode coupling in sound radiation from high-speed axisymmetric jets. *AIAA Paper* 2016-2803.

GOLDSTEIN, M. E., SESCU, A. & AFSAR, M. Z. 2012 Effect of non-parallel mean flow on the Green's function for predicting the low-frequency sound from turbulent air jets. *J. Fluid Mech.* **695**, 199–234.

GOLOVIZNIN, V. M. & SAMARSKII, A. A. 1998 Finite difference approximation of convective transport equation with space splitting time derivative. *J. Matem. Mod.* **10** (1), 86–100.

HUSSEIN, H. J., CAPP, S. P. & GEORGE, W. K. 1994 Velocity measurements in a high-Reynolds-number, momentum conserving, axisymmetric, turbulent jet. *J. Fluid Mech.* **258**, 31–75.

INGRAHAM, D. & BRIDGES, J. E. 2017 Validating a monotonically-integrated large eddy simulation code for subsonic jet acoustics. *AIAA Paper* 2017-0456.

KARABASOV, S. A. 2010 Understanding jet noise. *Phil. Trans. R. Soc. Lond.* A **368**, 3593–3608.

KARABASOV, S. A., AFSAR, M. Z., HYNES, T. P., DOWLING, A. P., MCMULLAN, W. A., PROKORA, C. D., PAGE, G. J. & MCGUIRK, J. J. 2010 Jet noise: acoustic analogy informed by large eddy simulation. *AIAA J.* **48** (7), 1312–1325.

KARABASOV, S. A., BOGEY, C. & HYNES, T. P. 2013 An investigation of the mechanisms of sound generation in initially laminar, subsonic jets using the Goldstein acoustic analogy. *J. Fluid Mech.* **714**, 24–57.

KARABASOV, S. A. & GOLOVIZNIN, V. M. 2009 Compact accurately boundary adjusting high-resolution technique for fluid dynamics. *J. Comput. Phys.* **228**, 7426–7451.

KARABASOV, S. A. & HYNES, T. P. 2006 Adjoint linearized Euler solver in the frequency domain for jet noise modelling. *AIAA Paper* 2006-2673.

KARABASOV, S. A. & SANDBERG, R. D. 2015 Influence of free stream effects on jet noise generation and propagation within the Goldstein acoustic analogy approach for fully turbulent jet inflow boundary conditions. *Intl J. Aeroacoust.* **14** (3–4), 413–430.

LAU, J. C, MORRIS, P. J. & FISHER, M. J. 1979 Measurements in subsonic and supersonic free jets using a laser velocimeter. *J. Fluid Mech.* **93** (1), 1–27.

LEIB, S. J. & GOLDSTEIN, M. E. 2011 Hybrid source model for predicting high-speed jet noise. *AIAA J.* **49** (7), 1324–1335.

LEIB, S. J., INGRAHAM, D. & BRIDGES, J. E. 2017 Evaluating source terms of the generalized acoustic analogy using the jet engine noise reduction (JENRE) code. *AIAA Paper* 2017-0459.

LIGHTHILL, M. J. 1952 On sound generated aerodynamically. Part I. General theory. *Proc. R. Soc. Lond.* **211** (1107), 564–587.

LILLEY, G. M. 1958 On the noise from air jets. *Aero. Res. Counc. R&M* **20**, 376.

MARKESTEIJN, A. P. & KARABASOV, S. A. 2018 CABARET solutions on graphics processing units for NASA jets: grid sensitivity and unsteady inflow condition effect. *C. R. Méc.* doi:10.1016/j.crme.2018.07.004.

MORRIS, P. J. & ZAMAN, K. B. M. Q. 2010 Velocity measurements in jets with application to noise source modeling. *J. Sound Vib.* **329**, 394–414.

NAJAFI-YAZDI, A., BRES, G. A. & MONGEAU, L. 2011 An acoustic analogy formulation for moving sources in uniformly moving media. *Proc. R. Soc. Lond.* A **467** (2125), 144–165.

POPE, S. B. 2000 *Turbulent Flows*. Cambridge University Press.

SAMANTA, A., FREUND, J. B., WEI, M. & LELE, S. K. 2006 Robustness of acoustic analogies for predicting mixing-layer noise. *AIAA J.* **44**, 2780–2786.

SEMILETOV, V. A. & KARABASOV, S. A. 2013 CABARET scheme with conservation-flux asynchronous time-stepping for nonlinear aeroacoustics problems. *J. Comput. Phys.* **253** (15), 157165.

SEMILETOV, V. A. & KARABASOV, S. A. 2014*a* Adjoint linearised Euler solver for Goldstein acoustic analogy equations for 3D non-uniform flow sound scattering problems: verification and capability study. *AIAA Paper* 2014-2318.

SEMILETOV, V. A. & KARABASOV, S. A. 2014*b* CABARET scheme for computational aero acoustics: extension to asynchronous time stepping and 3D flow modelling. *Intl J. Aeroacoust.* **13** (3–4), 321–336.

SEMILETOV, V. A. & KARABASOV, S. A. 2017 On the similarity scaling of jet noise sources for low-order jet noise modelling based on the Goldstein generalised acoustic analogy. *Intl J. Aeroacoust.* **16** (6), 476–490.

SEMILETOV, V. A., KARABASOV, S. A., CHINTAGUNTA, A. & MARKESTEIJN, A. P. 2015 Empiricism-free noise calculation from LES solution based on Goldstein generalized acoustic analogy: volume noise sources and meanflow effects. *AIAA Paper* 2015-2536.

SHUR, M. L., SPALART, P. R. & STRELETS, M. KH. 2005 Noise prediction for increasingly complex jets. Part I: methods and tests. Part II: applications. *Intl J. Aeroacoust.* **4** (3–4), 21366.

SHUR, M. L., SPALART, P. R., STRELETS, M. KH. & TRAVIN, K. T. 2015 An enhanced version of DES with rapid transition from RANS to LES in separated flows. *Turbulence Flow Combust.* **95** (4), 709737.

SILOET Programme. Rolls-Royce private data.

TAM, C. K. W. & AURIAULT, L. 1998 Mean flow refraction effects on sound from localized sources in a jet. *J. Fluid Mech.* **370**, 149–174.

TAM, C. K. W., VISWANATHAN, K., AHUJA, K. K. & PANDA, J. 2008 The sources of jet noise: experimental evidence. *J. Fluid Mech.* **615**, 253–992.

VISWANATHAN, K. 2004 Aeroacoustics of hot jets. *J. Fluid Mech.* **516**, 39–82.

VISWANATHAN, K. 2009 Mechanisms of jet noise generation: classical theories and recent developments. *Intl J. Aeroacoust.* **615**, 253–992.

WELCH, P. D. 1967 The use of fast Fourier transform for the estimation of power spectra: a method based on time averaging over short, modified periodograms. *IEEE Trans. Audio Electroacoust.* **15**, 70–73.

WITZE, P. O. 1974 Centerline velocity decay of compressible free jets. *AIAA J.* **12** (4), 417–418.